Simple femtosecond laser-based production of enlarged nickel surfaces alloyed with molybdenum, iron and cobalt using aqueous solutions and metal foils

Viktor Hoffmann [a,*], Luise Hoffmann [a], Wolfgang Schade [a,c], Thomas Turek [a,b], Thomas Gimpel [a,*]

[a] *Research Center Energy Storage Technologies, Clausthal University of Technology, EnergieCampus, Am Stollen 19A, 38640 Goslar, Germany*

[b] *Institute of Chemical and Electrochemical Process Engineering, Clausthal University of Technology, Leibnizstr. 17, 38678 Clausthal-Zellerfeld, Germany*

[c] *Fraunhofer Heinrich Hertz Institute, EnergieCampus, Am Stollen 19H, 38640 Goslar, Germany*

* Corresponding authors. E-mail addresses: viktor.hoffmann@tu-clausthal.de (V. Hoffmann), thomas.gimpel@tu-clausthal.de (T. Gimpel).

Keywords: femtosecond laser ablation, nickel alloy, surface structuring, molybdenum, cobalt, iron

Abstract

An entirely femtosecond laser (fs-laser) based process for the production of stable, enlarged and alloyed nickel surfaces is presented. The process allows the use of metal foils and aqueous salt solutions as alloying element sources. We alloy iron from an aqueous element source as well as molybdenum and cobalt from commercially available foils on nickel mesh surfaces without further coating process. It is shown that the content of alloyed iron on the nickel mesh surface structured with the fs-laser depends on the concentration of the aqueous iron(II) sulfate solution used. The alloy content of cobalt and molybdenum is controlled by adjustable laser parameters. Cross-sections prepared by a focused ion beam and subsequent energy dispersive X-ray spectroscopy shows that molybdenum and nickel form alloyed nanoscale particles on the structured nickel surface. The combination of an aqueous iron(II) sulfate solution and a molybdenum metal foil leads to a ternary nickel-molybdenum-iron surface alloy. The presented fs-laser alloying process can be applied to further metal combinations and offers the potential to create new materials and properties.

1. Introduction

The femtosecond laser (fs-laser) technology enables specific surface modifications of various materials such as metals [1,2], polymers [3,4], glasses [5,6], semiconductors [7,8] and crystalline solids [9]. The material surface is enlarged [10,11] and roughened [12] by fs-laser processing. This modification has an effect on various macroscopic material properties such as the wetting behavior [13,14], the reflectivity of electromagnetic radiation [15] and heat radiation [16]. In the field of alkaline water electrolysis, fs-laser structured electrodes cause an overvoltage reduction of the oxygen evolution reaction (OER) and the hydrogen evolution reaction (HER) [17–19]. The surface structures formed by laser-induced ablation and resolidification processes are characteristic and diverse [20–25]. Laser induced periodic surface structures (LIPSS), variously shaped holes, particles, threads and grooves on the nanometer scale, nanoparticles, but also cones and microgrooves up to the two-digit micrometer range are observed [26]. These structures can be controlled via laser parameters [11,27], the process environment [28], the material [29] and the angle of incidence of the fs laser beam [2,17]. LIPSS are formed on surfaces at fluences near the ablation threshold of the material, (e.g. for nickel between 0.1 and 0.2 J/cm²) [27,30]. This ablation threshold depends crucially on the process environment and the number of incident laser shots [27,30].

Conical microstructures will appear at a higher fluence or at an increased number of laser shots/spot [2,31,32]. Depending on the material, the size and the structures of the cones can also be manipulated via these parameters [31–33], while their surface density depends on the laser pulse width [34]. Furthermore, fs-lasers can also be used to introduce elements from process gases into solid surfaces [35,36] or to deposit aqueously dissolved salts on structured metal surfaces [37,38]. Fischer et al. [39] have shown that coatings of nanoscale alloyed ablation products are created with the fs-laser technology. This process requires a high vacuum system with rotating metal targets and is not designed to create the typical enlarged fs-laser-structured surfaces. However, these enlarged surfaces are of particular importance when the structured surface are used, e.g. in alkaline water electrolysis. As shown in [40], these structures contribute significantly to an improved electrolysis performance by reducing overvoltages. Alloys or coatings with catalyst materials enhance this effect. This has already been shown in the work of Koj et al. [18] for the OER and Gabler et al. [40] for the HER with fs-laser structured and coated electrodes.

In this work, a simple and exclusively fs-laser-based process for structuring and surface alloying of nickel meshes is presented for the first time. It enables the production of novel and stable alloys and represents an alternative to coating processes as described in [18] and [40]. Additionally, elemental compositions can be produced independently of the solid solubility limit [36]. Cobalt and molybdenum foils as well as aqueously dissolved iron(II) sulfate in various concentrations serve as alloying elements. The choice of the listed elements is based on future applications as electrode materials for alkaline water electrolysis [41].

2. Experimental

2.1 Material

Only nickel meshes are used as structuring and alloying objects (Ni 99.2 wt%, mesh size of 500 µm x 500 µm, thread thickness of 140 µm, sintered and wound to a thickness of 200 µm, Haver & Boecker from Germany). During all laser process steps the meshes are placed on structural supports made of solid nickel sheet (99.99 wt%, 1 mm thickness, 5 cm x 5 cm, Goodfellow from England) which are replaced after each alloying process. The metal foils for alloying are commercially available 50 µm thick molybdenum (99.95 wt %, HMW Hauner GmbH & Co. KG, Germany) and cobalt foils with the same thickness (99.9 wt %, HMW Hauner GmbH & Co. KG, Germany). Before use, the material thickness is reduced to 13 µm for Cobalt and 15 µm for Molybdenum by fs-laser ablation. The laser parameters of this ablation process are listed in the following section. As iron source aqueous solutions of iron(II) sulfate heptahydrate ($FeSO_4 \cdot 7\ H_2O$, MERCK, p. a.) are used, which are prepared with deionized water immediately before use.

2.2 Laser

The setup of the Ti:Sa based laser system consists of a Mantis seed laser from *Coherent* and a regenerative Spitfire amplifier from *Spectra Physics*. The complete laser system is described in [40]. An arrangement of mirrors and lenses directs the laser pulses into the sample chamber. This system generates laser pulses with a central wavelength of 800 nm and a single pulse width of about 60 fs. At a repetition rate (RR) of 10 kHz an average laser power up to 4 W is possible. Before the laser beam hits a sample, the power is reduced in a manually adjustable

attenuator and bundled by means of a focus lens with a focal length of 500 mm. A meandering scan is realized by two computer-controlled linear axes on which the focus lens is mounted. The linear scan speed is varied according to the number of laser shots/spot and the line pitch is set to 40 µm for all structuring processes. The spot diameter of the laser beam in the focus is determined with a commercial beam profiler to 78 µm ± 3 µm and has not been changed during all experiments. Within this diameter, the intensity of the Gaussian profile has decreased to 86.5% ($1/e^2$) from the center. The indicated deviation of the spot diameter results from the differences of the diameter in vertical and horizontal direction. Based on the settings the mean laser fluence applied on the sample is calculated to 5.4 J/cm² in the focus of the beam.

2.3 Sample Preparation

The process for manufacturing surface structured alloys can be divided into the following areas, which are shown schematically in Fig. 1: pre-structuring, application of the alloy source and alloying. Before laser processing, mesh and substrate are cleaned with 2-propanol and placed in the sample chamber according to the arrangement in Fig. 1 (a). The pre-structuring process for all samples consist of two runs of a meandering scan with a linear scan velocity of 10 mm/s according to about 100 laser shots/spot on an area of 5 x 5 mm² (Fig. 1 (b)). The increased roughness after the pre-structuring process facilitates subsequent structuring by an improved laser coupling and the application of aqueous solutions by an improved wetting.

In the case of the liquid element source, aqueous iron(II) sulfate concentration of 0.25, 0.2, 0.15, 0.1 and 0.05 g/mL are prepared. Then, 160 µL/cm² are applied with a syringe on the pre-structured area (Fig. 1 (c)). A cobalt or molybdenum metal foil must be placed firmly and without spacing on the mesh (Fig. 1 (d)). As shown in Fig. 1 (e), after the application step, the alloying step follows for all aqueous iron(II) sulfate solutions with one run of 100 laser shots/spot. In alloying steps of cobalt and molybdenum foils with a thickness of 13 µm and 15 µm, the number of incident laser shots/spot is varied between 200 and 300 in steps of 25. For alloying cobalt, an additional alloying step with 400 laser shots/spot and a 50 µm thick cobalt foil is shown. Furthermore, in a combined process two alloying elements are applied to the structured surface from an aqueous iron(II) sulfate solution with a concentration of 0.25 g/mL and a 15 µm thick molybdenum foil. Thus, after the pre-structure has been created, molybdenum is alloyed by 225 laser shots/spot and after the iron solution has been applied,

a second fs-laser process step at 100 laser shots/spot is carried out in a two-fold alloying step. All laser process steps are performed under a constant nitrogen (5.0, Linde) flow at a pressure of 660 mbar ± 20 mbar in a process chamber. Before SEM and EDX examination, all samples are cleaned with deionized water, acetone, 2-propanol and again with deionized water in an ultrasonic bath for 2 min each. Any loose ablation debris or iron salt residues are removed by this procedure.

The nickel-molybdenum alloys are referred to as NiLMo(x) and the nickel-cobalt alloys with NiLCo(x). The "L" represents the alloy of nickel by the laser process with molybdenum or cobalt while "x" represents the number of laser shots/spot applied for the alloying step. The nickel-iron alloys are referred to as NiLFe(y), where "y" stands for the concentration of the applied aqueous iron(II) sulfate solution in g/mL. The nickel-iron-molybdenum alloy NiLMoFe(225/0.25) is thus the result of a molybdenum alloy consisting of a 15 µm thick molybdenum foil processed with 225 laser shots/spot in the first alloying step and a subsequent alloying of iron from a 0.25 g/mL iron(II) sulfate solution with 100 laser shots/spot.

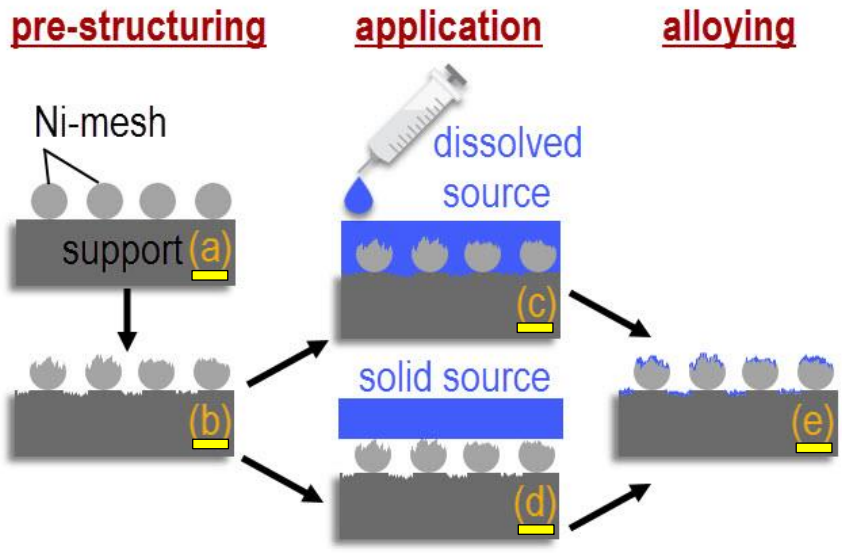

Figure 1: Scheme of the fs-laser-structuring and surface alloying process of nickel meshes. (a) Application of the Ni mesh on the solid support nickel sheet, (b) Ni mesh after pre-structuring by the fs-laser, (c) application of the liquid element source with a syringe or (d) application of the solid element source as metal foil on the pre-structured area, (e) alloying with a fs-laser process step.

2.4 Characterization

A scanning electron microscope (SEM) from Zeiss (EVO 50, MA10) is used for the morphological examination of the surface. Elemental analysis is performed by energy dispersive X-ray spectroscopy (EDX) using a Bruker Nano QUANTAX 800 system with an XFlash-6 detector. The EDX spectra and SEM images are captured with an acceleration voltage of 10 kV. In addition, a Helios Nanolab 600 from FEI is used to generate a cross-section of the sample NiLMo(225) with a focused ion beam (FIB). A subsequent SEM examination and several EDX-line profiles are performed at 10 kV.

3. Results and Discussion

Fig. 2 shows the SEM images at 1000- and 5000-fold magnification of the alloys NiLCo(300), NiLCo(400), NiLFe(0.25), NiLMo(300), NiLMoFe(225/0.25). The surfaces of NiLCo(300) and NiLCo(400), which are shown in Fig. 2 (a-d), consist of cone-like and prismatically-shaped microstructures with a length of up to 30 µm. These structures are exclusively interspersed with LIPSS as shown in white frames in Fig. 2 for every alloy. The conical microstructures in Fig. 2 (e+f) of the NiLFe(0.25) surface are formed with diameters between 10 µm and 20 µm. The conical surface is covered with LIPSS which are highlighted with a white frame in Fig. 2 (e) and ablation products in the form of microparticles like in Fig. 2 (e). Structurally, this surface strongly resembles the fs-laser-structured and iron-coated nickel surface of Koj et al. [18]. Because the laser parameters and surface structures are identical to the structure in [18], it can be concluded that the alloying process from an aqueous solution does not inhibit the fs-structuring on the nickel mesh.

Fig. 2 (g+h) shows the NiLMo(300) flattened conical microstructures in the order of 10 to 20 µm. The submicrostructure of this alloy consists mainly of nanoscale particles and areas of LIPSS. In the submicrometer range, the surface of NiLMoFe(225/0.25) is also equipped with particulate nanostructures and LIPSS (Fig. 2 (i+j)). On the microstructure level an inhomogeneous picture results for the ternary alloy, since there are surface areas with and without conical structures. In summary, especially the submicrostructure of the fs-laser-alloyed nickel surfaces depends on the alloying element. Nanoparticles occur in molybdenum-

alloyed nickel surfaces. The submicrostructure of the cobalt-alloyed nickel surfaces consists exclusively of LIPSS. Surfaces alloyed with iron show mainly LIPSS and some microparticles.

The results of the elemental analysis of the alloyed nickel surfaces are shown in Fig. 3. The mean atomic concentration is plotted with the standard deviation for each sample as a function of the iron(II) sulfate concentration for the iron alloys (upper abscissa). For the cobalt and molybdenum alloys the mean atomic concentration is plotted against the number of laser shots/spots in the alloying step (lower abscissa). The listed results are based on nine measurements at defined positions of the mesh for each parameter set. For each position the EDX measurement is performed at 1000-fold magnification integrating over an area element of about 75 µm x 110 µm in order to provide comparability.

Fig. 3 shows that the average molybdenum content on a structured nickel surface increases from 8.3 to 14.6 at.% if the number of laser shots/spot in the alloying step is increased from 200 to 300. Between 200 and 225 laser shots/spot, the average molybdenum content increases by 2.1 at.%, while between 225 and 250 laser shots/spot the increase is only 0.1 at.%. This is followed by a change of 1.2 at.% when the number of laser shots/spot rises from 250 to 275. The largest increase occurs between 275 and 300 laser shots/spot with 2.8 at.%. From these results, it is concluded that the average amount of molybdenum can be controlled by the number of laser shots/spot in the alloying step of the fs-laser process. For more than 300 laser shots/spot, the mechanical stability of the nickel mesh is no longer given.

The mean iron content of the NiLFe sample series increases from 5.8 to 11.3 at.% when the Fe(II)SO_4(aq) concentration is changed from 0.05 to 0.25 g/mL. Thus, a fivefold increase in the iron concentration causes only a doubling of the average alloyed iron content on a structured nickel surface. The mean absolute deviations range from ± 2.7 at.% at a concentration of 0.05 g/mL to ± 1.6 at.% at 0.15 g/mL, which is less than the deviation of the molybdenum alloy. The changes in the alloying quantities also differ between the Fe(II)SO_4 concentrations. A doubling of the concentration from 0.05 to 0.1 g/mL results in an increase of 2.7 at.% in the amount of alloyed iron. An increase from 0.1 to 0.15 g/mL results in an increase of 1.9 at.%. Between 0.15 and 0.2 g/mL Fe(II)SO_4 (aq) even a reduction of 0.2 at.% of iron is observed, whereas between 0.2 and 0.25 g/mL an increase of only 1.3 at.% occurs. This graphical course indicates a saturation behavior. Nevertheless, for the alloying of iron from an aqueous

$Fe(II)SO_4$ solution, it can be summarized that the amount of iron alloyed on a structured nickel surface can be controlled by the iron concentration in an aqueous solution.

For the NiLCo series only at 225 laser shots/spot a maximum of 2.7 at.% is achieved, while the minimum is 1.5 at.% and occurs at 300 laser shots/spot. Thus, no influence is clearly determined for the amount of cobalt alloying from a 13 µm thick cobalt foil. The differences in the quantity of molybdenum or cobalt on a structured nickel surface is clearly attributed to the element in this experiment. However, processing a 50 µm thick cobalt foil on the nickel substrate at 400 laser shots/spot in the alloying step results in sample NiLCo(400) with a cobalt content of 8.6 $\pm$ 1.9 at.%. This proves that the amount of the alloying element on a structured surface depends on adequate laser parameters.

The performance of the fs-laser alloying process is demonstrated with the NiLMoFe(225/0.25) alloy. This alloy shows both an iron content of up to 9.7 at.% together with a molybdenum content of up to 5.2 at.% within a nickel matrix. Ternary structured surface compounds are thus accessible without additional sample preparation or complex coating procedures. Only one additional fs-laser process step is required.

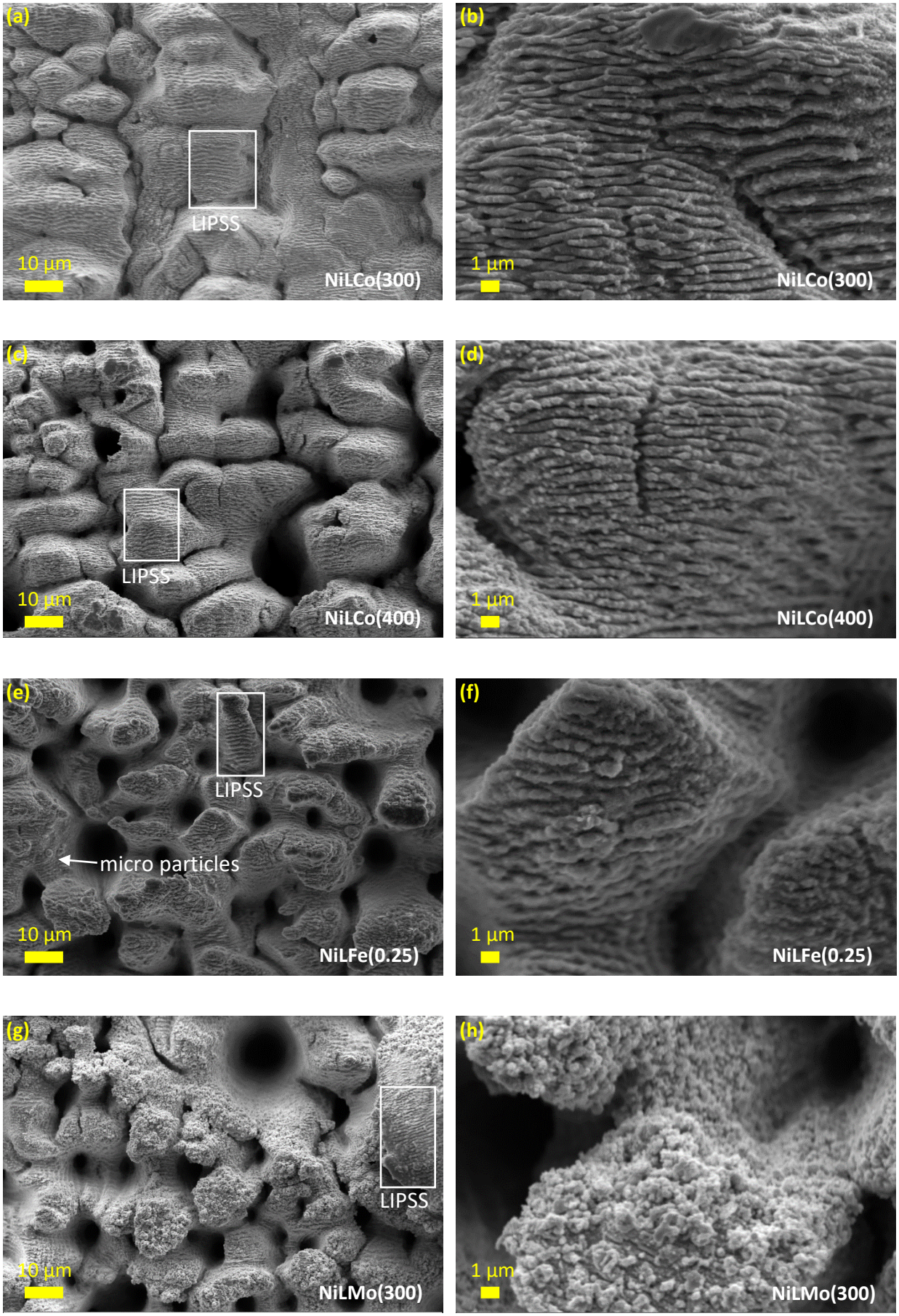
(a)
LIPSS
10 µm
NiLCo(300)
(b)
1 µm
NiLCo(300)
(c)
LIPSS
10 µm
NiLCo(400)
(d)
1 µm
NiLCo(400)
(e)
LIPSS
micro particles
10 µm
NiLFe(0.25)
(f)
1 µm
NiLFe(0.25)
(g)
LIPSS
10 µm
NiLMo(300)
(h)
1 µm
NiLMo(300)

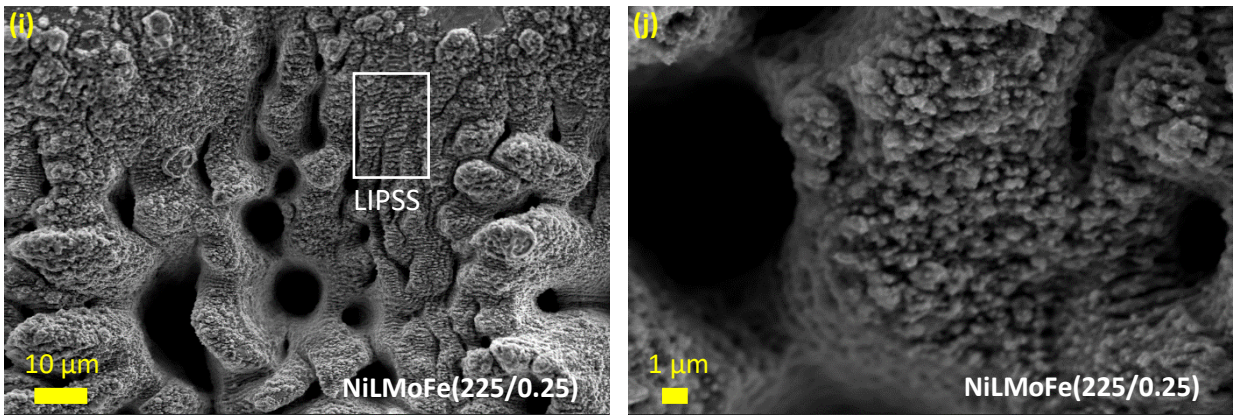

Figure 2: SEM images at 1000- and 5000-fold magnification for NiLCo(300) (a+b), NiLCo(400) (c+d), NiLFe(0.25) (e+f), NiLMo(300) (g+h) and NiLMoFe(225/0.25) (i+j).

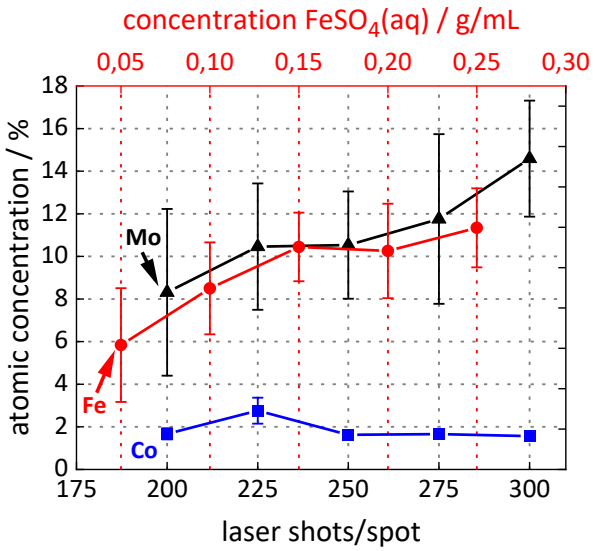

Figure 3: Atomic concentration of molybdenum (triangles) and cobalt (squares) on a structured nickel surface as a function of the laser shots/spot for the alloying step (bottom abscissa) and of iron (circles) as a function of the Fe(II)SO_4(aq) concentration (top abscissa).

Fig. 4 (a) shows the SEM image of a FIB cross-section of the NiLMo(225) surface. The lines of the three EDX-line profiles A, B and C are shown from 0 µm to 1.25 µm in the enlarged areas of the cross-section in Fig. 4 (b) and the results of the EDX-line profiles in Fig. 4 (c). The diagrams show in black lines the atomic fraction of nickel and molybdenum in red lines as a function of the distance from the surface. The FIB cross-section in Fig. 4 (a+b) shows that the surface of NiLMo(225) consists of nanoscale particles and elevations. This surface is chosen similar to the surface of NiLMo(300) in Fig. 2 (g+h). Thus, the elevations correspond to the LIPSS and do not show any visible boundaries to the subsurface. In contrast, visible boundaries highlight the particles forming nanoporous cavities. For clarification, the bottom particle edges in Fig. 4 (b) are highlighted with blue lines in the diagrams of Fig. 4 (c). In the course of

the EDX-line profile A, molybdenum contents of 62 at.% within the first particle and even 67 at.% at the bottom particle edge are reached at 0.7 µm. Below the edge of the particle, the molybdenum content drops continuously until a distance of about 1 µm below 10 at.%. A similar behavior is obtained for the second particle from the EDX-line profile B. Within the particle length of 0.4 µm, two maximum molybdenum proportions of 47 at.% and 38 at.% are achieved. The molybdenum content begins to drop already within the particle after the second maximum of 38 at.% at 0.4 µm. After a distance of about 0.75 µm, the molybdenum fraction further drops to almost 5 at.%.

The third particle in EDX-line profile C reaches a maximum molybdenum content of 64 at.% at 0.25 µm and then falls at 0.4 µm directly to 20 at.%, then gradually to 10 at.% at 0.7 µm, which is the edge of the particle. Finally, within the substrate the molybdenum content discontinuously falls below 3 at.% at about 1.0 µm. The intersection of the molybdenum and nickel fraction corresponding to an atomic ratio of approx. 1:1, occur in the range of < 1 µm twice each for the EDX-line profiles B and C and four times for A. This type of particulate alloy formation using an fs-laser is consistent with the results of Fischer et al. [39].

The following four statements are deduced:

1. Nickel and molybdenum coexist at each position studied, which suggests binary metal alloys with different atomic ratios.
2. The highest molybdenum content is present in the form of alloyed and re-solidified nanoparticles, which are formed by the fs-laser alloying process. The more particles are present on a surface element, the greater is the molybdenum content in this area.
3. Higher molybdenum contents occur in the bulk surface within a very thin layer of 0.2 µm to 0.4 µm, which continuously decreases towards the bulk. This indicates a diffusion of the element of ablation debris on the surface towards the bulk.
4. The particles are chemically and mechanically stable on the structured nickel surface, because the cleaning procedure in an ultrasonic bath does not remove the particles.

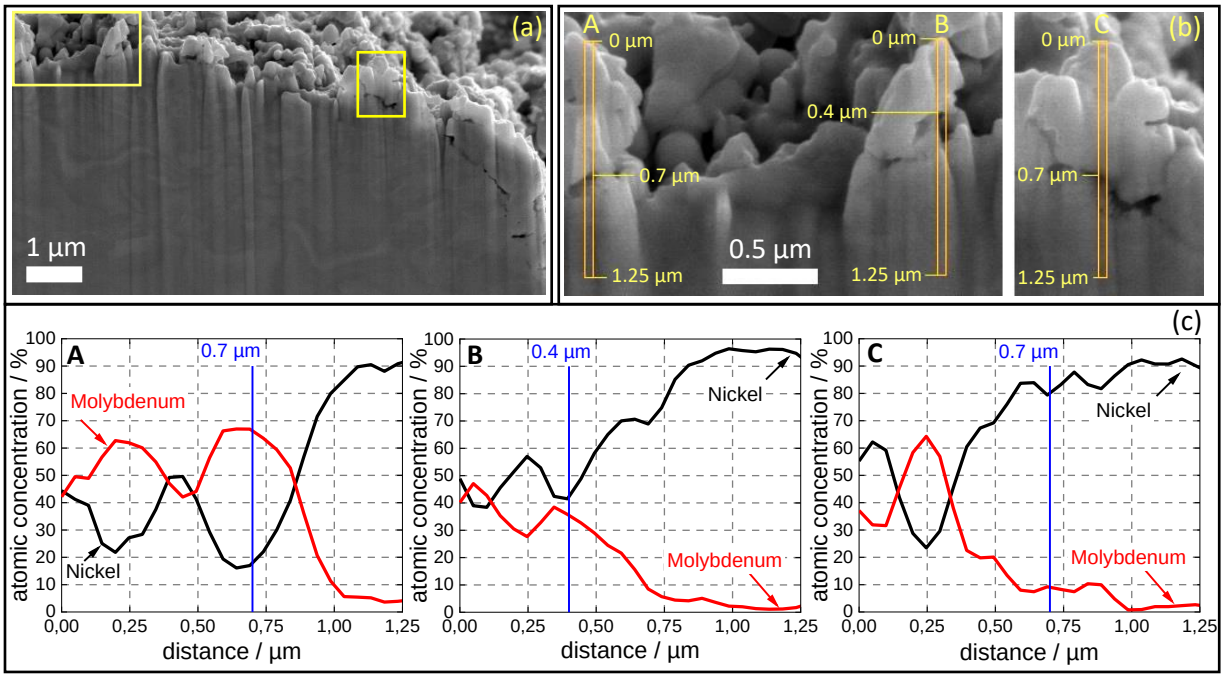

Figure 4: SEM image of a FIB cross-section of NiLMo(225) at a cone in (a), magnified areas with the EDX-line profiles A, B and C in (b) which are highlighted with yellow rectangles in (a), EDX diagrams of the line profiles with the element concentration of nickel as black lines and molybdenum as red lines as a function of the distance. Bottom particle edges within the line profiles are highlighted at 0.7 µm, 0.4 µm and 0.7 µm in (b) and as blue lines in (c).

4. Conclusion

In this work, a simple fs-laser-based process for the production of stable, enlarged and metal-alloyed surface structures on nickel is presented for the first time. It consists of a structuring and alloying process. With this process, different alloying element sources like metallic cobalt and molybdenum foils but also aqueous dissolved Fe(II)SO_4 salts are used. An additional coating of the substrate is not necessary.

Aqueous Fe(II)SO_4 solutions in concentrations of 0.05 to 0.25 g/mL lead to iron alloys on the structured nickel surfaces with average iron contents between 5.8 and 11.3 at.%. This average iron content is dependent on the Fe(II)SO_4 concentration, whereby a saturation behavior develops between 0.15 and 0.25 g/mL. The surface of NiLFe alloys consists of conical microstructures, which are mainly covered with LIPSS and partially with microparticles. The liquid alloying source does not disturb the structure formation on the nickel mesh. Comparable surface structures are also observed by Koj et al. [18] on fs-laser-structured nickel-iron alloys.

The cobalt and molybdenum content on a structured and laser-alloyed nickel surface are controlled by the number of laser shots/spot in the alloying step. For the molybdenum alloys, average proportions of 8.3 to 14.6 at.% result and for cobalt alloys a content up to 8.6 at.% is achieved. The amount of alloying element on a structured nickel surface depends on the alloying element itself and the laser parameters. On the microstructure level, conical spikes up to 30 µm in length are observed for all binary surface alloys. The submicrostructure shows exclusively LIPSS for the NiLCo alloys. On the NiLMo- and the ternary alloyed NiLMoFe(225/0.25) surfaces, nanoscale particles and areas with LIPSS are increasingly found. The alloying element thus significantly influences the surface structure of the nickel mesh. EDX-line profiles of the cross-section of a NiLMo(225) surface show that the nanoscale and particulate re-solidified ablation products are the main carriers of molybdenum. The more particles are present on a surface element, the greater is the molybdenum content in this area. The alloying elements of the iron and cobalt alloys thus appear differently from the molybdenum alloys on the structured nickel surfaces.

The ternary NiLMoFe(225/0.25) alloy demonstrates the capability of the fs-laser alloying process. It is produced from different element sources without additional sample preparation and coating processes. Molybdenum contents of up to 5.2 at.% and simultaneous iron contents of up to 9.7 at.% are achieved within the ternary nickel alloy. In general, all desired metal combinations come into consideration to be alloyed by this method.

Acknowledgements

We would like to thank Dr. René Gustus from Clausthal Centre for Material Technology (CZM) for creating the FIB cross-section. This work was funded by the German Research Foundation (DFG) under the project number 397568108.

References

[1] A.Y. Vorobyev, V.S. Makin, C. Guo, Periodic ordering of random surface nanostructures induced by femtosecond laser pulses on metals, J. Appl. Phys. 101 (2007) 34903. https://doi.org/10.1063/1.2432288.

[2] T.Y. Hwang, C. Guo, Polarization and angular effects of femtosecond laser-induced conical microstructures on Ni, J. Appl. Phys. 111 (2012) 83518. https://doi.org/10.1063/1.4704394.

[3] M. Forster, W. Kautek, N. Faure, E. Audouard, R. Stoian, Periodic nanoscale structures on polyimide surfaces generated by temporally tailored femtosecond laser pulses, Phys. Chem. Chem. Phys. 13 (2011) 4155–4158. https://doi.org/10.1039/c0cp01798a.

[4] B.T. Least, D.A. Willis, Modification of polyimide wetting properties by laser ablated conical microstructures, Appl. Surf. Sci. 273 (2013) 1–11. https://doi.org/10.1016/j.apsusc.2012.12.141.

[5] V.R. Bhardwaj, E. Simova, P.P. Rajeev, C. Hnatovsky, R.S. Taylor, D.M. Rayner, P.B. Corkum, Optically Produced Arrays of Planar Nanostructures inside Fused Silica, Phys. Rev. Lett. 96 (2006) 57404. https://doi.org/10.1103/PhysRevLett.96.057404.

[6] S. Höhm, A. Rosenfeld, J. Krüger, J. Bonse, Femtosecond laser-induced periodic surface structures on silica, J. Appl. Phys. 112 (2012) 14901. https://doi.org/10.1063/1.4730902.

[7] A. Borowiec, H.K. Haugen, Subwavelength ripple formation on the surfaces of compound semiconductors irradiated with femtosecond laser pulses, Appl. Phys. Lett. 82 (2003) 4462–4464. https://doi.org/10.1063/1.1586457.

[8] F. Costache, S. Kouteva-Arguirova, J. Reif, Sub–damage–threshold femtosecond laser ablation from crystalline Si: surface nanostructures and phase transformation, Appl. Phys. A 79 (2004) 1429–1432. https://doi.org/10.1007/s00339-004-2803-y.

[9] F. Costache, M. Henyk, J. Reif, Surface patterning on insulators upon femtosecond laser ablation, Appl. Surf. Sci. 208-209 (2003) 486–491. https://doi.org/10.1016/S0169-4332(02)01443-5.

[10] A.R. Neale, Y. Jin, J. Ouyang, S. Hughes, D. Hesp, V. Dhanak, G. Dearden, S. Edwardson, L.J. Hardwick, Electrochemical performance of laser micro-structured nickel oxyhydroxide cathodes, J. Power Sources 271 (2014) 42–47. https://doi.org/10.1016/j.jpowsour.2014.07.167.

[11] B.K. Nayak, M.C. Gupta, Self-organized micro/nano structures in metal surfaces by ultrafast laser irradiation, Opt. Laser Eng. 48 (2010) 940–949. https://doi.org/10.1016/j.optlaseng.2010.04.010.

[12] A.-M. Kietzig, S.G. Hatzikiriakos, P. Englezos, Patterned Superhydrophobic Metallic Surfaces, Langmuir 25 (2009) 4821–4827. https://doi.org/10.1021/la8037582.

[13] J. Lu, T. Huang, Z. Liu, X. Zhang, R. Xiao, Long-term wettability of titanium surfaces by combined femtosecond laser micro/nano structuring and chemical treatments, Appl. Surf. Sci. 459 (2018) 257–262. https://doi.org/10.1016/j.apsusc.2018.08.004.

[14] P. Bizi-bandoki, S. Valette, E. Audouard, S. Benayoun, Time dependency of the hydrophilicity and hydrophobicity of metallic alloys subjected to femtosecond laser irradiations, Appl. Surf. Sci. 273 (2013) 399–407. https://doi.org/10.1016/j.apsusc.2013.02.054.

[15] A.Y. Vorobyev, C. Guo, Colorizing metals with femtosecond laser pulses, Appl. Phys. Lett. 92 (2008) 41914. https://doi.org/10.1063/1.2834902.

[16] C. Gerhard (Ed.), S. Wieneke (Ed.), W. Viöl (Ed.), Laser ablation: Fundamentals, methods and applications, Nova Science Publishers Inc., New York, 2015.

[17] F. Rieck genannt Best, J. Koch, G. Lilienkamp, F. Körkemeyer, H.J. Maier, J. Caro, K. Lange, Spiky Nickel Electrodes for Electrochemical Oxygen Evolution Catalysis by Femtosecond Laser Structuring, Int. J. Electrochem 2018 (2018) 1–12. https://doi.org/10.1155/2018/9875438.

[18] M. Koj, T. Gimpel, W. Schade, T. Turek, Laser structured nickel-iron electrodes for oxygen evolution in alkaline water electrolysis, Int. J. Hydrogen Energ. 44 (2019) 12671–12684. https://doi.org/10.1016/j.ijhydene.2019.01.030.
[19] A. Gabler, C.I. Müller, T. Rauscher, M. Köhring, B. Kieback, L. Röntzsch, W. Schade, Ultrashort pulse laser-structured nickel surfaces as hydrogen evolution electrodes for alkaline water electrolysis, Int. J. Hydrogen Energ. 42 (2017) 10826–10833. https://doi.org/10.1016/j.ijhydene.2017.02.006.
[20] S.I. Anisimov, B.S. Luk'yanchuk, Selected problems of laser ablation theory, Phys.-Usp. 45 (2002) 293–324. https://doi.org/10.1070/PU2002v045n03ABEH000966.
[21] I.N. Zavestovskaya, A.P. Kanavin, N.A. Men'kova, Crystallization of metals under conditions of superfast cooling when materials are processed with ultrashort laser pulses, J. Opt. Technol. 75 (2008) 353–358. https://doi.org/10.1364/JOT.75.000353.
[22] S. I. Anisimov, B. L. Kapeliovich, T. L. Perel'man, Electron emission from metal surfaces exposed to ultrashort laser pulses, Zh. Eksp. Teor. Fiz. 66 (1974) 776–781.
[23] N.M. Bulgakova, A.V. Bulgakov, Pulsed laser ablation of solids: transition from normal vaporization to phase explosion, Appl. Phys. A 73 (2001) 199–208. https://doi.org/10.1007/s003390000686.
[24] D. Perez, L.J. Lewis, Ablation of Solids under Femtosecond Laser Pulses, Phys Rev Lett 89 (2002) 255504. https://doi.org/10.1103/PhysRevLett.89.255504.
[25] M. Ishino, A.Y. Faenov, M. Tanaka, N. Hasegawa, M. Nishikino, S. Tamotsu, T.A. Pikuz, N.A. Inogamov, V.V. Zhakhovsky, I.Y. Skobelev, V.E. Fortov, V.A. Khohlov, V.V. Shepelev, T. Ohba, T. Kaihori, Y. Ochi, T. Imazono, T. Kawachi, Nanoscale surface modifications and formation of conical structures at aluminum surface induced by single shot exposure of soft x-ray laser pulse, J. Appl. Phys. 109 (2011) 13504. https://doi.org/10.1063/1.3525980.
[26] A.Y. Vorobyev, C. Guo, Direct femtosecond laser surface nano/microstructuring and its applications, Laser Photonics Rev. 7 (2013) 385–407. https://doi.org/10.1002/lpor.201200017.
[27] S. Preuss, A. Demchuk, M. Stuke, Sub-picosecond UV laser ablation of metals, Appl. Phys. A 61 (1995) 33–37. https://doi.org/10.1007/BF01538207.
[28] J. Lehr, F. de Marchi, L. Matus, J. MacLeod, F. Rosei, A.-M. Kietzig, The influence of the gas environment on morphology and chemical composition of surfaces micro-machined with a femtosecond laser, Appl. Surf. Sci. 320 (2014) 455–465. https://doi.org/10.1016/j.apsusc.2014.09.011.
[29] T.Y. Hwang, A.Y. Vorobyev, C. Guo, Ultrafast dynamics of femtosecond laser-induced nanostructure formation on metals, Appl. Phys. Lett. 95 (2009) 123111. https://doi.org/10.1063/1.3222937.
[30] P.T. Mannion, J. Magee, E. Coyne, G.M. O'Connor, T.J. Glynn, The effect of damage accumulation behaviour on ablation thresholds and damage morphology in ultrafast laser micro-machining of common metals in air, Appl. Surf. Sci. 233 (2004) 275–287. https://doi.org/10.1016/j.apsusc.2004.03.229.
[31] A.Y. Vorobyev, C. Guo, Femtosecond laser structuring of titanium implants, Appl. Surf. Sci. 253 (2007) 7272–7280. https://doi.org/10.1016/j.apsusc.2007.03.006.
[32] A.Y. Vorobyev, C. Guo, Femtosecond laser nanostructuring of metals, Opt. Express 14 (2006) 2164–2169. https://doi.org/10.1364/OE.14.002164.
[33] E. Stratakis, A. Ranella, C. Fotakis, Biomimetic micro⁄nanostructured functional surfaces for microfluidic and tissue engineering applications, Biomicrofluidics 5 (2011) 13411. https://doi.org/10.1063/1.3553235.

[34] V. Zorba, N. Boukos, I. Zergioti, C. Fotakis, Ultraviolet femtosecond, picosecond and nanosecond laser microstructuring of silicon: structural and optical properties, Appl. Opt. 47 (2008) 1846–1850. https://doi.org/10.1364/AO.47.001846.
[35] R. Younkin, J.E. Carey, E. Mazur, J.A. Levinson, C.M. Friend, Infrared absorption by conical silicon microstructures made in a variety of background gases using femtosecond-laser pulses, J. Appl. Phys. 93 (2003) 2626–2629. https://doi.org/10.1063/1.1545159.
[36] K.-M. Guenther, T. Gimpel, S. Kontermann, W. Schade, Investigation of the sulfur doping profile in femtosecond-laser processed silicon, Appl. Phys. Lett. 102 (2013) 202104. https://doi.org/10.1063/1.4807679.
[37] X. Lin, X. Li, G. Li, Y. Zhang, Z. Cui, Micro-dot-matrix induced by femtosecond laser on titanium surface for Ca-P phase deposition, Appl. Surf. Sci. 499 (2020) 143925. https://doi.org/10.1016/j.apsusc.2019.143925.
[38] Y. Yang, J. Yang, C. Liang, H. Wang, X. Zhu, N. Zhang, Surface microstructuring of Ti plates by femtosecond lasers in liquid ambiences: a new approach to improving biocompatibility, Opt. Express 17 (2009) 21124–21133. https://doi.org/10.1364/OE.17.021124.
[39] D. Fischer, G.F. de La Fuente, M. Jansen, A new pulsed laser deposition technique: Scanning multi-component pulsed laser deposition method, Rev. Sci. Instrum. 83 (2012) 43901. https://doi.org/10.1063/1.3697861.
[40] A. Gabler, C.I. Müller, T. Rauscher, T. Gimpel, R. Hahn, M. Köhring, B. Kieback, L. Röntzsch, W. Schade, Ultrashort-pulse laser structured titanium surfaces with sputter-coated platinum catalyst as hydrogen evolution electrodes for alkaline water electrolysis, Int. J. Hydrogen Energ. 43 (2018) 7216–7226. https://doi.org/10.1016/j.ijhydene.2018.02.130.
[41] F. Safizadeh, E. Ghali, G. Houlachi, Electrocatalysis developments for hydrogen evolution reaction in alkaline solutions – A Review, Int. J. Hydrogen Energ. 40 (2015) 256–274. https://doi.org/10.1016/j.ijhydene.2014.10.109.